IEEE Open Journal of the Industrial Electronics Society

Received 30 April 2020; revised 3 July 2020; accepted 19 July 2020. Date of publication 27 July 2020; date of current version 17 August 2020. The review of this article was arranged by Editor Z. Zhang.

Digital Object Identifier 10.1109/OJIES.2020.3011926

Performance Benchmarking of a Novel Magnet-Free Bearingless Synchronous Reluctance Slice Motor

THOMAS HOLENSTEIN [1] (Student Member, IEEE), MARCEL SCHUCK [2] (Member, IEEE), AND JOHANN W. KOLAR [2] (Fellow, IEEE)

(Invited Paper)

[1]Levitronix GmbH, 8005 Zurich, Switzerland
[2]Power Electronic Systems Laboratory, ETH Zurich, 8092 Zurich, Switzerland

CORRESPONDING AUTHOR: MARCEL SCHUCK (e-mail: schuck@lem.ee.ethz.ch)

ABSTRACT This paper presents a novel bearingless synchronous reluctance slice motor topology that contains no permanent magnets. The rotor with two iron poles and flux barriers is levitated and rotated through a stator winding system with six coils wired as two three-phase systems. A constant rotor-oriented magnetization current is applied to generate a magnetic bias flux. The system can be controlled similar to a bearingless permanent magnet synchronous slice motor and provides passive stabilization of axial and tilting movements of the rotor. The motor topology is discussed in detail and a prototype implementation is presented. Its performance with regard to passive properties, achievable torque, controllability, and wide air gap suitability is benchmarked against two other designs that contain permanent magnets either in the rotor or the stator. A loss analysis of all topologies is performed and suitable application areas are identified. The proposed design provides an interesting alternative to existing bearingless slice motor topologies in applications that require high rotational speeds, high process or ambient temperatures, or a disposable low-cost rotor with short exchange intervals.

INDEX TERMS Bearingless slice motor, synchronous reluctance motor, magnet-free motor, topology benchmarking, wide air gap machines.

I. INTRODUCTION

Bearingless motors feature a magnetically levitated rotor and a stator with a magnetically integrated bearing function [1]. The same iron circuit is used for torque and radial force generation with either a separated or combined winding system [2]. If the stator and rotor lengths are chosen to be much smaller than the rotor diameter to form a slice motor, only the two radial degrees of freedom have to to be actively stabilized apart from the rotation [3].

A significant advantage of bearingless slice motors is that the rotor can be separated and isolated from the stator in a simple manner. Contactless rotation in a hermetically sealed containment is possible over a wide operating range, making such motors well suited for ultra-pure, low-shear fluid handling; harsh environmental conditions, such as aggressive chemicals; abrasive media; or extreme ambient temperatures. To leverage this advantage, a thick process chamber wall that is resistant to pressure, heat, and chemicals is required between the stator and the rotor, resulting in a wide air gap in the range of several millimeters. A schematic drawing of such an arrangement in a mixing application is provided in Fig. 1.

Many conventional motor topologies can also be configured as bearingless motors [4]. Bearingless motors have undergone a similar evolution as mechanically supported electrical machines with a delay of several years due to the added complexity. Bearingless induction and reluctance motors were initially demonstrated in the 1990s [5], and followed by rotor permanent magnet (PM) topologies [6], [7], as soon as strong PM materials became widely available. More recently, stator-PM topologies have also been demonstrated [8].

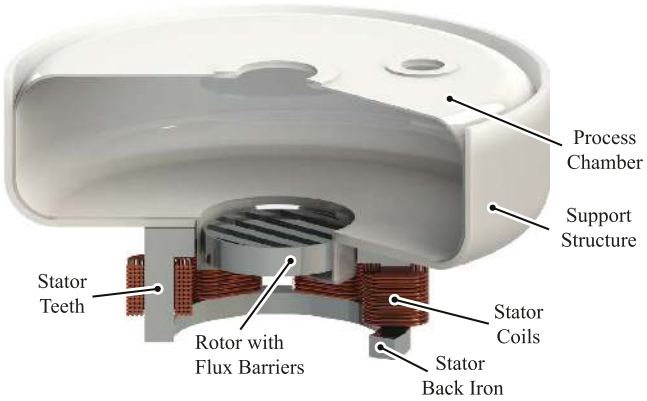

FIGURE 1. Application scenario of the proposed bearingless synchronous reluctance slice motor with rotor flux barriers.

Modern 3D finite element method (FEM) simulation capabilities and inverter technology have lead to a reconsideration of synchronous reluctance motors (SynRM) [9], [10]. This development was also driven by the rare-earth price rally in 2011 and has led to commercially available magnet-free motors that feature rotor flux barriers and achieve competitive efficiencies (IE4, super-premium efficiency level class) [11], [12].

Bearingless SynRM with flux barriers were first introduced in [13]. Compared to reluctance topologies with salient rotor poles [14], more linear torque and force generation with small fluctuations over the rotor angle were observed. Additionally, almost no coupling between force and torque generation exists, which facilitates stable bearing operation without a decoupling control algorithm such as needed for salient-pole topologies.

The proposed machine topology is easy to control as the control algorithms are identical to those of a rotor-PM machine. The only required modification is to set a constant magnetization current $I_{\mathrm{mag}} = I_{\mathrm{drv,d}}$ that is zero in the case of rotor-PM machines, where $I_{\mathrm{drv,d}}$ denotes a drive current that is oriented in the d-axis of a rotor-oriented coordinate system. A variety of recent works deal with the bearingless operation of SynRM with flux barriers [15]–[19]. A single slice motor concept completely without PMs that relies on an additional premagnetization coil has been published in [20]. Recently, a bearingless SynRM with a combination of salient rotor poles and flux barriers as well as combined windings has been presented [21].

This paper presents the design and implementation of a completely magnet-free bearingless SynRM with a focus on aspects that are specific to slice motors, namely passive axial and tilting stabilization. The switched-off motor is completely non magnetic. This simplifies its handling significantly, e.g., the rotor can be removed without having to overcome forces caused by PMs. The performance of the proposed motor topology is benchmarked against two bearingless flux switching permanent magnet (FSPM) slice motor topologies with PMs in the stator that were presented in [22] as well as a rotor-PM bearingless synchronous slice motor. The complete omission of PMs in the proposed motor topology

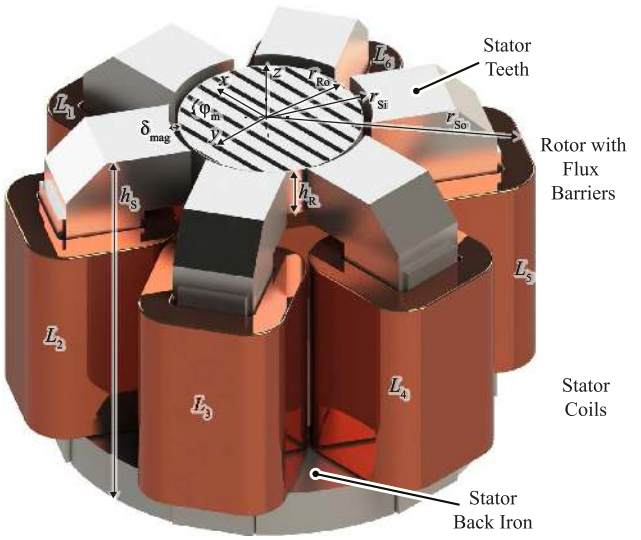

FIGURE 2. Rendering of the introduced bearingless six-slot, two-pole SynRM slice motor with rotor flux barriers and six concentrated motor windings for combined torque and radial force generation.

is found to be advantageous for high operating temperatures at which the performance of PM materials are degraded, high rotational speeds, and low manufacturing costs of the rotor. Moreover, the design facilitates a significantly higher radial startup distance and improved controllability compared to the FSPM topology. This work is a significant extension to [23], which presented initial design considerations for such a motor topology.

The remainder of this paper is organized as follows: Section II presents the motor topology, its design procedure, control scheme, and shows a prototype implementation of the proposed SynRM. Section III provides an overview of the topologies with PMs either in the rotor or the stator against which the implemented machine is benchmarked. Section IV presents a detailed comparison of the achievable performance of all four considered motor topologies with regard to passive properties, active force and torque generation, as well as controllability. Moreover, a rating regarding the suitability of the individual topologies for different applications is outlined. Finally, Section V concludes the paper.

II. SYNCHRONOUS RELUCTANCE SLICE MOTOR

A. TOPOLOGY AND GEOMETRY

The proposed entirely PM-free bearingless synchronous reluctance slice motor topology is shown in Fig. 2. A SynRM can be implemented with a rotor featuring teeth or flux barriers. Using a rotor with flux barriers results in a homogeneous magnetic flux distribution and, consequently, a more constant generation of forces and torque over an entire revolution, compared to the use of rotor teeth. This effect is particularly pronounced for the presented design with a two-pole reluctance rotor with nine straight parallel flux barriers. The resulting low electrical frequency facilitates low iron losses and makes the design suitable for high speed rotation [24], [25]. This is an advantage over SynRM with conventional ball bearings, in

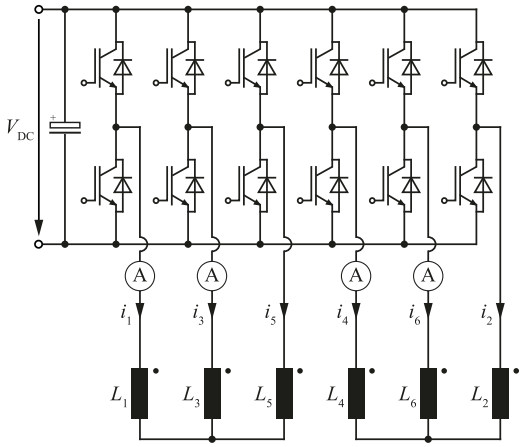

FIGURE 3. Connection scheme of the six motor windings to the employed six-phase inverter.

which rotors with at least two pole pairs have to be used to provide sufficient space for the motor shaft in the radial center of the machine [11].

Six stator teeth, each with a concentrated motor winding for combined generation of torque, radial bearing forces, and premagnetization of the machine are used. Such a setup results in improved thermal properties and low stray fields. The stator teeth are connected by a circular back-iron located at the lower end of the stator. This decreases the required outer diameter of the machine and is commonly referred to as a temple motor design.

In order to accommodate a process chamber wall that is resistant to pressure, heat, and chemicals, a relatively large magnetic air gap is required. For the subsequent considerations, a ratio of the air gap to rotor radius

$$G = \frac{\delta_{\mathrm{mag}}}{r_{\mathrm{Ro}}} = \frac{r_{\mathrm{Si}}}{r_{\mathrm{Ro}}} - 1 \tag{1}$$

of 0.1 is used, where δ_{mag}, r_{Ro}, and r_{Si} denote the magnetic air gap length, the outer rotor radius, and the inner stator radius, respectively (cf. Fig. 2). This value is similar to that used in existing bearingless motor topologies with rotors featuring PMs [26], [27].

To ensure that axial and tilting movements of the rotor are passively stabilized by the magnetic bias field that is generated by the constant magnetization current I_{mag}, the ratio

$$H = \frac{h_{\mathrm{R}}}{d_{\mathrm{Ro}}} = \frac{h_{\mathrm{R}}}{2r_{\mathrm{Ro}}} \tag{2}$$

is chosen as 0.26, where h_{R} and d_{Ro} denote the rotor height and rotor diameter, respectively. The stated value was obtained from 3D magnetostatic FEM simulations to maximize the stiffness against tilting movements of the rotor.

B. WINDING LAYOUT AND CURRENT GENERATION

The six motor windings are connected as two three-phase systems with a floating star point each and are powered by a six-phase inverter, as shown in Fig. 3. This arrangement is commonly used (see e.g., [28]) and only four current sensors are required to control all currents, since $i_1 + i_3 + i_5 = 0$ and $i_4 + i_6 + i_2 = 0$ holds.

The available four degrees of freedom are used to control the radial position of the rotor in the x and y directions, the rotational speed ω_{m} and the magnetization current I_{mag}. A superimposed control algorithm is used to generate setpoint values for the virtual bearing and drive currents $I_{\mathrm{bng,x}}$, $I_{\mathrm{bng,y}}$, and $I_{\mathrm{drv,q}}$, which are directly proportional to the radial forces F_{x}, F_{y} and the motor torque T_{m}, respectively, for a given magnetization current $I_{\mathrm{mag}} = I_{\mathrm{drv,d}}$.

Equation (3) describes how the momentary virtual bearing and drive currents are transformed and added to generate the six combined motor winding currents i_1 to i_6, where the matrix K is defined in (4). The considered coordinate system is shown in Fig. 2. The mechanical rotor angle is denoted by φ_{m} from which the electrical rotor angle can be obtained as $\varphi_{\mathrm{e}} = p_{\mathrm{rot}}\varphi_{\mathrm{m}}$, where p_{rot} denotes the pole pair number of the rotor. For the proposed SynRM the relation $p_{\mathrm{drv}} = p_{\mathrm{rot}} = 1$ and $p_{\mathrm{bng}} = p_{\mathrm{drv}} \pm 1 = 2$ has to hold, similar to bearingless permanent magnet synchronous motors (PMSM). The pole pair number and topology configurations can easily be adjusted in software.

$$\begin{bmatrix} i_1 \\ i_2 \\ i_3 \\ i_4 \\ i_5 \\ i_6 \end{bmatrix} = K(p_{\mathrm{drv}}) \cdot \begin{bmatrix} i_{\mathrm{drv,d}} \\ i_{\mathrm{drv,q}} \end{bmatrix} + K(p_{\mathrm{bng}}) \cdot \begin{bmatrix} i_{\mathrm{bng,x}} \\ i_{\mathrm{bng,y}} \end{bmatrix} \tag{3}$$

$$K(p) = \begin{bmatrix} \cos(\varphi_{\mathrm{e}}) & \cos(\varphi_{\mathrm{e}} + \frac{\pi}{2}) \\ \cos(\varphi_{\mathrm{e}} - p\frac{\pi}{3}) & \cos(\varphi_{\mathrm{e}} - p\frac{\pi}{3} + \frac{\pi}{2}) \\ \cos(\varphi_{\mathrm{e}} - p\frac{2\pi}{3}) & \cos(\varphi_{\mathrm{e}} - p\frac{2\pi}{3} + \frac{\pi}{2}) \\ \cos(\varphi_{\mathrm{e}} - p\frac{3\pi}{3}) & \cos(\varphi_{\mathrm{e}} - p\frac{3\pi}{3} + \frac{\pi}{2}) \\ \cos(\varphi_{\mathrm{e}} - p\frac{4\pi}{3}) & \cos(\varphi_{\mathrm{e}} - p\frac{4\pi}{3} + \frac{\pi}{2}) \\ \cos(\varphi_{\mathrm{e}} - p\frac{5\pi}{3}) & \cos(\varphi_{\mathrm{e}} - p\frac{5\pi}{3} + \frac{\pi}{2}) \end{bmatrix} \tag{4}$$

Nonlinearities (e.g., due to saturation effects) are not accounted for in the torque and position control. In order to achieve stable levitation of the rotor, the magnetomotive force (MMF) needs to be chosen such that no strong saturation occurs. This does not impose a significant restriction, as saturation is also undesirable with regard to motor losses.

C. PASSIVE STABILIZATION, RADIAL FORCE, AND TORQUE

To illustrate the underlying mechanism of force generation in the motor, a simplified rectangular magnetic circuit with constant cross-sectional area A_{Fe}, iron length l_{Fe}, two air gaps with lengths l_δ, and a coil with N turns wound around the magnetic circuit and carrying a current I is considered. If it is further assumed that there is no stray flux and that the field lines cross the air gap over the same cross section as the iron circuit ($A_{\mathrm{Fe}} = A_\delta$), the following relationship between the MMF $\Theta = NI$ in ampere turns (AT) and the magnetic field is

obtained:

$$\oint H \cdot \mathrm{d}s = l_{\mathrm{Fe}} H_{\mathrm{Fe}} + 2 l_\delta H_\delta = l_{\mathrm{Fe}} \frac{B}{\mu_0 \mu_{\mathrm{r}}} + 2 l_\delta \frac{B}{\mu_0} = \Theta. \quad (5)$$

Solving (5) for B and assuming infinite permeability of the iron ($\mu_{\mathrm{r}} \to \infty$), it can be seen that the magnetic flux density is proportional to the coil current divided by the air gap length:

$$B = \mu_0 \frac{NI}{\frac{l_{\mathrm{Fe}}}{\mu_{\mathrm{r}}} + 2 l_\delta} \approx \mu_0 \frac{\Theta}{2 l_\delta}. \quad (6)$$

The force acting on the two air gaps is proportional to B^2 (7) and, therefore, also to I^2, according to (6) (refer to e.g., [29], Chapter 3 for more details).

$$F = \frac{B^2 A_{\mathrm{Fe}}}{\mu_0} \approx \frac{\mu_0 A_{\mathrm{Fe}} N^2 I^2}{2 {l_\delta}^2} \quad (7)$$

Based on this simplified model, it can be seen that a magnetization current I_{mag} leads to attracting forces between the stator teeth and the rotor of the considered SynRM topology that increase quadratically with I_{mag}. The sum of these forces is zero for a centered rotor due to (3) and (4).

Passive restoring forces that pull the rotor back towards the axial center of the stator are generated in case of an axial deflection or tilting by an angle α or β around the magnetization axis (d-axis) or the axis perpendicular to the magnetization (q-axis), respectively. These restoring forces increase linearly with the deflection, and the mechanical stiffnesses

$$k_z = \frac{\mathrm{d}F_z}{\mathrm{d}z} \qquad k_\alpha = \frac{\mathrm{d}T_\alpha}{\mathrm{d}\alpha} \qquad k_\beta = \frac{\mathrm{d}T_\beta}{\mathrm{d}\beta} \quad (8)$$

can be defined for a given value of I_{mag}, where $k_\alpha < k_\beta$ holds. For a radial deflection, a destabilizing force that pulls the rotor away from the stator center is obtained and the corresponding stiffnesses

$$k_{\mathrm{x}} = -\frac{\mathrm{d}F_{\mathrm{x}}}{\mathrm{d}x} \qquad k_{\mathrm{y}} = -\frac{\mathrm{d}F_{\mathrm{y}}}{\mathrm{d}y} \quad (9)$$

have a negative value.

It can be seen form the reluctance motor torque equation

$$T = \frac{3}{2} p_{\mathrm{drv}} (L_{\mathrm{d}} - L_{\mathrm{q}}) I_{\mathrm{drv,d}} I_{\mathrm{drv,q}} \quad (10)$$

that the motor torque increases linearly with $I_{\mathrm{drv,q}}$ and $I_{\mathrm{drv,d}}$. Here, L_{d} and L_{q} denote the machine inductance along the d and q axis, respectively.

Radial forces increase linearly with I_{bng} and I_{mag}, which is best illustrated by the forces of two opposing stator teeth being added to form the resulting radial force, e.g., in accordance with Fig. 2, $F_{\mathrm{x},1} = F_{\mathrm{coil1}} + F_{\mathrm{coil4}}$ at $\varphi_{\mathrm{m}} = 0^\circ$, yielding

$$F_{\mathrm{x},1} \propto (I_{\mathrm{mag}} + I_{\mathrm{bng,x}})^2 - (I_{\mathrm{mag}} - I_{\mathrm{bng,x}})^2 = 4 I_{\mathrm{mag}} I_{\mathrm{bng,x}}. \quad (11)$$

Equation (11) is based on a flux density and radial bearing force that increase in a linear and quadratic manner with the MMF, respectively. This only holds true under the simplification of a linear material behavior (neglecting saturation effects). Moreover, for slice motors with a wide air gap, as in the considered case, the simplified model without stray flux and straight field lines within the air gap does not hold true any more. Considerable stray flux paths between the stator teeth as well as below and above the motor exist. Consequently, the magnitude of the B-field within the air gap and the rotor is lower than expected, while it is higher than expected in the iron below the coils. Saturation occurs earlier and forces are lower than in the simplified model. In order to take these effects into account, 3D FEM simulations have to be used to obtain sufficiently precise values for the forces and torque. Nevertheless, the outlined proportionality relations are still valid.

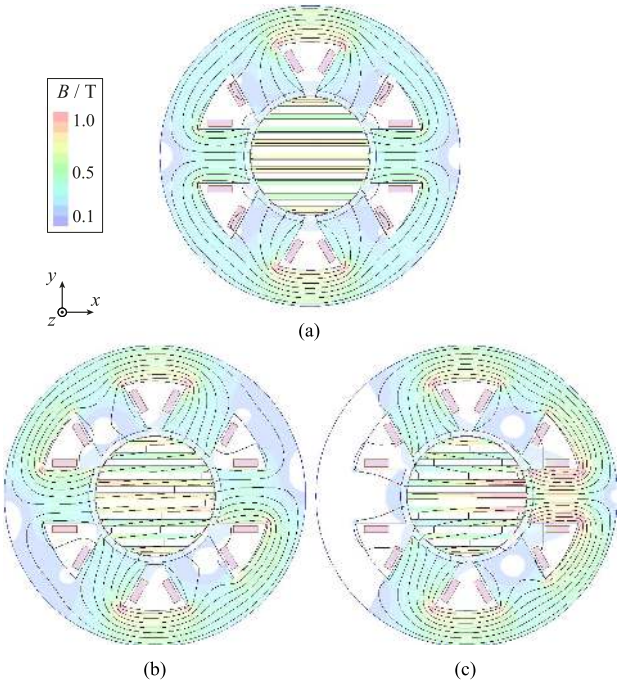

FIGURE 4. Magnetic flux density and flux lines inside the bearingless SynRM shown for: (a) a magnetization flux ($\Theta_{\mathrm{mag}} = 1500$ AT), (b) torque generation ($\Theta_{\mathrm{drv,q}} = \Theta_{\mathrm{mag}} = 1500$ AT), and (c) radial force generation ($\Theta_{\mathrm{bng,x}} = \Theta_{\mathrm{mag}} = 1500$ AT).

Fig. 4 shows the flux lines in the bearingless SynRM for the three scenarios of a magnetization current only (a), torque generation (b), and radial force generation (c). It can be seen that the flux density inside the stator teeth is proportional to the applied current. For a pure magnetization current, the flux lines do not cross the flux barriers. Crossing of the flux barriers results in a bearing force or reluctance torque.

If the motor is oriented such that the rotor is positioned horizontally (cf. Fig. 2), the gravitational force acting on the rotor is counteracted by the passive axial stiffness as outlined in (8) and results in a small vertical deflection. If the motor is oriented such that the rotor is positioned vertically, the gravitational force (constant disturbance force) needs to be counteracted by the radial bearing forces.

D. MAGNETIZATION CURRENT CONSIDERATIONS

Due to the quadratic relation between the overall coil current and the forces and torque, the SynRM topology is expected

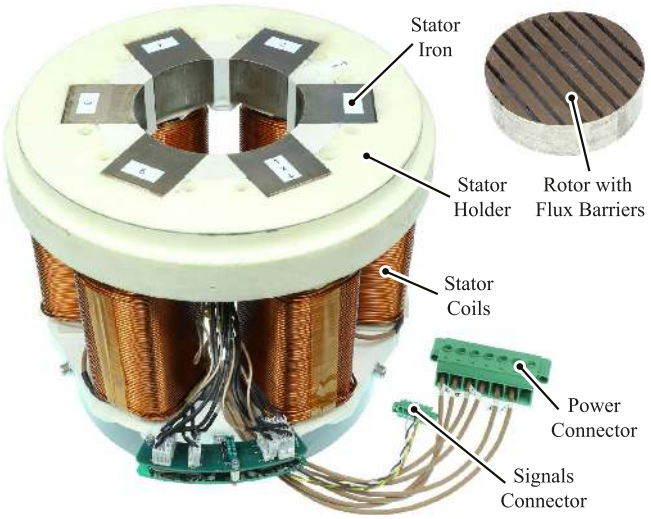

FIGURE 5. Annotated photograph of the implemented prototype of the proposed entirely permanent-magnet-free bearingless SynRM with removed housing. The single pole-pair rotor with straight flux barriers is shown separately.

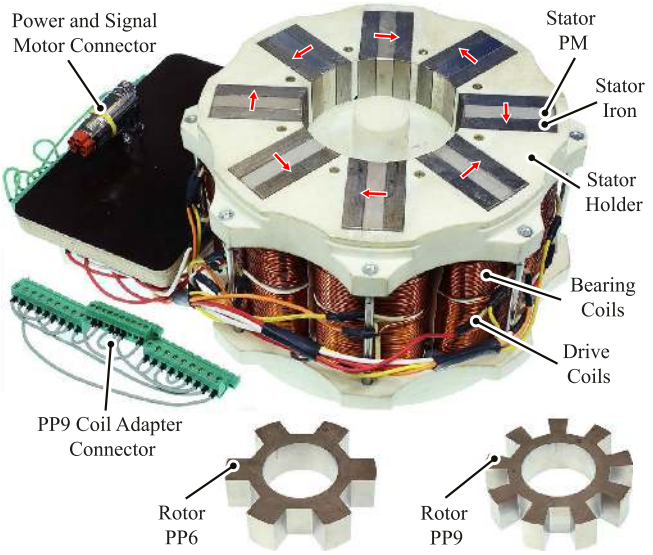

FIGURE 6. Eight slot FSPM motor with stator permanent magnets (magnetization directions shown by red arrows). The stator contains separated windings for generating the drive torque and magnetic bearing force. The stator can be used in conjunction with either the shown six pole pair or nine pole pair PM-free rotor.

to exhibit superior performance compared to PM topologies for a high MMF. The maximum torque per current is achieved for $I_{\mathrm{mag}} = I_{\mathrm{drv,d}} = I_{\mathrm{drv,q}}$, i.e., for a drive current angle of 45°. This results in ohmic idle losses caused by the magnetization current that are half of the full load losses.

The capability of adjusting the magnetization current during operation provides several possibilities, namely:

- Dynamic adjustment of the axial steady-state position.
- Improved damping of axial oscillations compared to PM motors (e.g., [30]).
- Avoidance of resonances during run up through dynamic adjustment of the passive stiffnesses.
- Variable prioritization of high dynamic performance and low iron losses, e.g., for high speed operation. A high magnetization current can be used to achieve a high dynamic performance at the cost of high losses, e.g., for acceleration/deceleration. Contrarily, high rotational speeds can be achieved at low losses for a low magnetization current, at the cost of poor dynamic behavior.

It should be noted that field weakening in PM machines could be used to achieve a similar behavior, however, within significantly narrower limits.

E. PROTOTYPE

Fig. 5 shows the implemented prototype of the proposed SynRM. In order to increase mechanical stability, the prototype is implemented with 3D-printed mechanical support structures at the upper and lower vertical ends of the stator. The back iron and the rotor are manufactured from axially sheeted electrical steel, while the stator teeth are made from tangentially sheeted electrical steel. If desired, the same stator could be used in combination with a four-pole reluctance rotor.

III. BENCHMARKING TOPOLOGIES WITH PERMANENT MAGNETS

The performance of the proposed SynRM topology is benchmarked against three other slice motor topologies with PMs either in the rotor or in the stator [31]. In order for the motors to be comparable, identical rotor diameters as well as ratios for G and H according to (1) and (2) are used.

A. FLUX-SWITCHING MACHINE WITH STATOR PERMANENT MAGNETS

Fig. 6 shows the FSPM slice motor design with PMs in the stator that was presented in [22]. The stator consists of eight teeth that each contain a tangentially-magnetized PM with alternating magnetization directions (marked by red arrows in Fig. 6). In contrast to the proposed SynRM design, separate drive and bearing windings are used for generating the torque and magnetic bearing force, respectively.

The PM-free rotor, as shown in Fig. 6, has either six (FSPM PP6) or nine (FSPM PP9) teeth. This corresponds to six or nine pole pairs, respectively, as each rotor tooth yields identical characteristics in front of the same stator tooth for which the bias flux is determined by the respective stator PM. An adapter connector is used to adjust the wiring to either generate a stator field with $p_{\mathrm{drv}} = 6$ and $p_{\mathrm{bng}} = 7$ for the FSPM PP6, or $p_{\mathrm{drv}} = 9$ and $p_{\mathrm{bng}} = 10$ for the FSPM PP9.

Similar to the SynRM, the back iron and the rotor are manufactured from axially sheeted electrical steel, while the stator teeth are made from tangentially sheeted electrical steel. The PMs are glued to the center of the stator teeth. Due to the tangentially magnetized stator magnets, this topology mostly generates tangential forces (in contrast to radial forces

TABLE I Geometrical Parameters, Material Volumes, and Masses of the Four Benchmarked Motor Topologies

		SynRM	FSPM		PMSM
			PP6	PP9	
d_{Ro}	mm	100	100		100
h_{R}	mm	26	26		26
δ_{mag}	mm	5	5		5
d_{So}	mm	287	247		203
h_{S}	mm	193	164		170
$V_{\mathrm{S,Fe}}$	cm^3	3190	1870		1510
$V_{\mathrm{S,Cu}}$	cm^3	1880	507		702
$V_{\mathrm{S,PM}}$	cm^3	–	641		–
$m_{\mathrm{S,Fe}}$	kg	24.4	14.3		11.6
$m_{\mathrm{S,Cu}}$	kg	16.8	4.54		6.29
$m_{\mathrm{S,PM}}$	kg	–	4.81		–
V_{R}	cm^3	157	94.2	91.4	124.6
m_{R}	kg	1.2	0.72	0.7	0.94

in the PM and the SynRM machines). Therefore, this topology is highly effective at generating torque. However, it is less effective at generating the required bearing forces in the radial direction.

B. SYNCHRONOUS MACHINE WITH ROTOR PERMANENT MAGNETS

The stator of the considered bearingless PMSM has an identical topology to that of the SynRM depcited in Fig. 5, however, with significantly reduced material volumes. The rotor consists of eight radially magnetized PMs that are glued to a back iron in order to minimize the reluctance. This arrangement results in a rotor field with four pole pairs. The stator currents for this machine are generated according to (3) and (4) with $p_{\mathrm{drv}} = 4$ and $p_{\mathrm{bng}} = 5$, while $I_{\mathrm{mag}} = 0$ as the bias flux is generated by the PMs.

The relevant geometrical parameters, material volumes, and masses for all motor designs are listed in Table I. It can be seen that significant differences regarding the use of PM material exist. While the proposed SynRM uses no PM material, the FSPM employs almost 5 kg of PM material in the stator. The considered PMSM employs approximately one tenth of this mass in the rotor. It can also be observed that the overall stator volume, the copper volume, and the iron volume of the SynRM are more than two times higher than for the PMSM.

IV. RESULTS

The following performance comparison is carried out based on the aforementioned mixing application that requires a high rotor torque density and high passive axial and tilting stiffnesses at relatively low rotational speeds [32], [33]. As such motors are usually limited by thermal constraints, the torque and active radial forces are compared at the same motor losses, which consist mostly of ohmic winding losses, while iron losses are at a negligible level due to the low rotational speeds. To obtain the magnetic bias flux that is necessary for

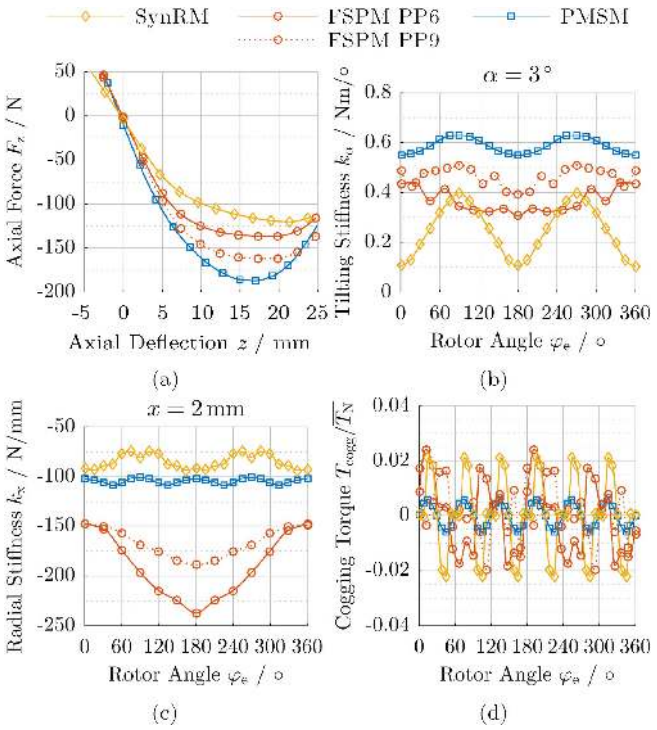

FIGURE 7. Passive axial restoring force versus axial deflection (a), tilting stiffness k_α for a tilting angle of $\alpha = 3°$ (b), destabilizing passive radial stiffness for an axial deflection of $x = 2$ mm (c), and normalized cogging torque (d) of the implemented prototypes. The results for the SynRM were obtained for the nominal magnetization flux $\Theta_{\mathrm{mag,N}}$ =2850 AT.

the passive stabilization of the rotor, the SynRM generates half of the ohmic full-load losses, while the PMSM and FSPM topologies both generate no ohmic losses. In order to provide a comprehensive analysis, the motors are compared regarding their passive forces and torques, active forces and drive torque, as well as the controllability of the magnetic bearing. The results were obtained by 3D FEM electromagnetic simulations at varying rotor angles, axial rotor deflections, and different MMFs. The material properties of N45 grade neodymium-iron-boron magnets and magnetic steel M330-35A were used for all simulations. All simulations were carried out using the magnetostatic solver (no eddy currents) of Ansys Maxwell with automatic meshing.

A. PASSIVE STIFFNESSES AND COGGING TORQUE

Passive stabilization of the axial position z and the two tilting degrees of freedom, α and β, is achieved with the rotor or stator PMs for the PMSM and the FSPM topology, respectively. For the introduced SynRM, passive stabilization is achieved through the bias flux that is generated by the current I_{mag}.

The axial restoring force is mostly independent of the rotor angle and is shown for all topologies versus the axial deflection of the rotor in Fig. 7(a). While the axial stiffness as described by (8) is similar for all topologies around zero, it decreases more rapidly for the SynRM and FSPM, resulting in a lower load capacity of the rotor.

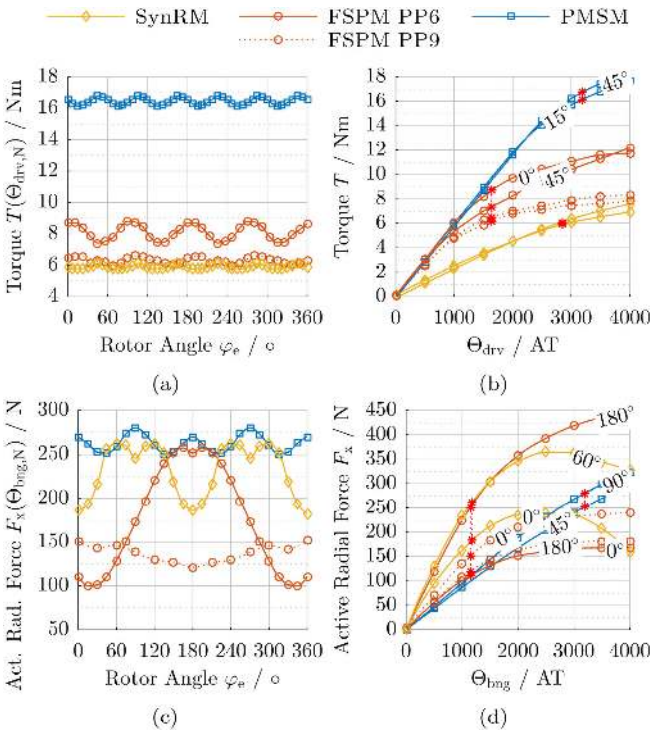

FIGURE 8. Motor torque versus rotor angle at nominal drive flux $\Theta_{drv,N}$ (a), torque for different values of Θ_{drv} (b), active radial force versus rotor angle at nominal bearing flux $\Theta_{bng,N}$ (c), and active radial force for different values of Θ_{bng} (d) of the implemented prototypes. The nominal flux values are listed in Table II and are marked by red asterisks in subfigures (b) and (d). The characteristics shown in (b) and (d) have been obtained for the two rotor angles at which their extreme values are reached. The corresponding values of φ_e are listed next to the respective curves.

The passive tilting stiffness versus the rotor angle is shown in Fig. 7(b) for a tilting angle of $\alpha = 3°$. It can be seen that the difference in the tilting stiffnesses around the d- and q-axis is more pronounced for a small pole pair number (e.g., the SynRM), while it is almost negligible for the FSPM topology. A big difference between k_α and k_β can be problematic at low rotational speeds since the tilting eigenfrequencies are more easily excited by disturbances.

The destabilizing passive radial stiffness versus the rotor angle is shown in Fig. 7(c) for a radial deflection of the rotor of 2 mm. Contrary to the tilting stiffness, large variations can be observed for the FSPM topology, while the radial stiffness is relatively constant for the SynRM and PMSM topologies.

Fig. 7(d) shows the ratio of the cogging torque and the average nominal torque versus the rotor angle. As a result of the conducted geometrical optimizations for all topologies, the cogging toque is below 2.5% of the nominal torque, making it irrelevant for the desired applications.

B. ACTIVE FORCES AND TORQUE

Fig. 8 shows the torque generation and active radial force properties of the implemented prototypes. It can be observed that a similar design in which the nominal flux values coincide with the onset of saturation was chosen for all motors. It can be seen that the PMSM topology provides a torque that is at least twice as high as that of the other topologies. Additionally, the radial force is more constant and has a higher average value at the nominal flux. The FSPM PP6 topology exhibits a large fluctuation of the active radial force over the rotor angle, which negatively affects its controllability (see below). As shown in Fig. 8(d), the SynRM exhibits a decreasing radial force for $\Theta_{bng} > 2500$ AT, which is attributed to saturation effects.

TABLE II Nominal Flux Values, Passive and Active Properties Averaged Over One Revolution of the Rotor

		SynRM	FSPM		PMSM
			PP6	PP9	
$\Theta_{mag,N}$	AT	2850	0		0
$\Theta_{drv,N}$	AT	2850	1640		3190
$\Theta_{bng,N}$	AT	1180	1150		3190
$\overline{k_z}(\Theta_{mag,N})$	N/mm	10.2	14.1	15.6	19.9
$\overline{k_{\alpha,\beta}}(\Theta_{mag,N})$	Nm/°	0.25	0.37	0.44	0.59
$\overline{k_r}(\Theta_{mag,N})$	N/mm	84.6	193	168	105
$\overline{T}(\Theta_{drv,N})$	Nm	5.90	8.10	6.30	16.4
$\overline{F_{r,act}}(\theta_{bng,N})$	N	233	170	136	262

Table II summarizes passive and active properties of all topologies. The overline indicates that the listed values are averaged over one revolution of the rotor. The listed axial stiffness was obtained for an axial deflection of ±6 mm. While this is rather large (≈ 25% of the rotor height), such values can occur in applications in which static or dynamic (e.g., mixing) axial forces are exerted on the rotor.

All properties were obtained for the listed nominal flux values. In order to provide a fair comparison, $\Theta_{drv,N}$ and $\Theta_{bng,N}$ were chosen such that they result in ohmic losses of 200 W each for all topologies. During operation, the full bearing and drive currents are never applied at the same time. In case of combined windings, drive and bearing currents are added and subtracted in an alternating manner, which results in an overall flux that is only marginally higher than that obtained for a pure drive current. As a result, overall ohmic losses of 200 W can be assumed during operation. In case of the SynRM topology, $\Theta_{mag,N}$ has to be applied continuously and results in ohmic losses of 100 W (conditions under which values in Table II were obtained). Ohmic losses of 200 W result from the combination with $\Theta_{drv,N}$ and $\Theta_{bng,N}$, where the overall flux is $\sqrt{2} \cdot 2850$ AT $= 4030$ AT. For the FSPM topology with separated windings, the overall ohmic losses are obtained as the sum of the losses in the drive and the bearing windings, resulting in lower values for $\Theta_{drv,N}$ and $\Theta_{bng,N}$ in order to remain at the loss limit of 200 W.

Considering the material volumes and masses listed in Table I, it is apparent that the SynRM provides lower volumetric and gravimetric torque densities than the benchmarking topologies. However, it exhibits the lowest manufacturing costs (despite the high copper volume) of all topologies since it uses no rare-earth PMs. This makes it highly suitable for

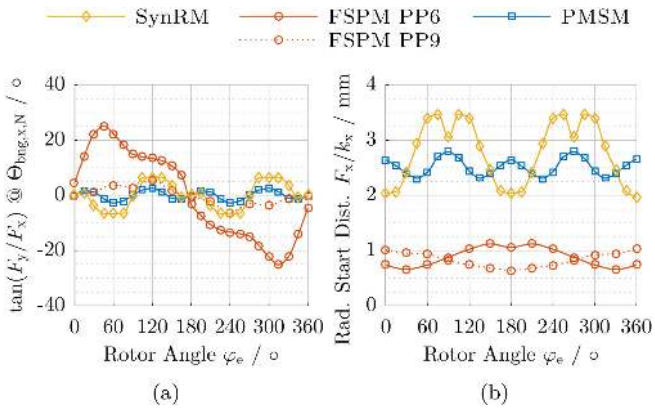

FIGURE 9. Deviation angle between the desired and the actual radial bearing force (a), and maximum admissible radial startup distance (b) versus the rotor angle.

rotor disposable applications (see below) and provides advantages at high operating temperatures at which demagnetization of PMs would occur.

C. CONTROLLABILITY

As stated above, the controllability of the FSPM PP6 is compromised by the large fluctuations of the active radial force. An additional controllability metric is the deviation angle between the desired and the actual radial bearing force, as shown in Fig. 9(a). While the PMSM and FSPM PP9 topologies exhibit similar performance with a slight inferiority of the SynRM, the FSPM PP6 shows angle deviations of up to 25°. Due to the uneven number of rotor poles, the FSPM PP9 topology additionally exhibits a parasitic radial force with a magnitude of up to 45% of the averaged desired radial force if a drive current is applied. The aforementioned fluctuations in the active radial force and the force angle have to be accounted for by feed-forward control in order to attain stable levitation of the rotor.

Fig. 9(b) shows the maximum distance for which a startup procedure of the motor is possible for different rotor angles. The startup distance in an application has to be chosen such that $F_x(\varphi_m) > k_x(\varphi_m) \cdot x \quad \forall \varphi_m$ has to hold. The distance for which this is fulfilled is low for the FSPM topologies, due to the combination of low active radial forces and a high destabilizing passive radial stiffness. The latter is caused by the PMs in the stator and requires a high bandwidth position controller for successful stabilization of the rotor.

A quantitative summary of this section is provided in Table III, where critical characteristics are marked in red. The fluctuation of the drive torque and the cogging torque is at a negligible level and does not need to be compensated in the desired applications. Overall, the best performance and controllability are achieved with the PMSM topology. The proposed SynRM topology exhibits favorable controllability characteristics entirely without PMs. However, the achievable torque and passive tilting stiffnesses are lower than for the PMSM. While the FSPM topologies provide passive axial and tilting stiffnesses that are only slightly below those of the PMSM, significant disadvantages exist regarding their control and the achievable torque is only slightly higher than for the SynRM.

TABLE III Controllability Metrics for the Implemented Prototypes: (a) Fluctuation of the Drive Torque, (b) Normalized Cogging Torque, (c) Fluctuation of the Active Radial Force, (d) Angular Deviation of the Active Radial Force, (e) Normalized Parasitic Radial Force Due to a Drive Current, (f) Minimum and (g) Maximum Startup Distance, (h) Fluctuation of the Tilting Stiffness

	SynRM	FSPM		PMSM
		PP6	PP9	
(a) ΔT_N	±2.9%	±8.5%	±5.2%	±1.9%
(b) $T_{cogg} / \overline{T_N}$	±2.1%	±2.4%	±1.8%	±0.6%
(c) $\Delta F_{r,act,N}$	±17%	±44%	±11%	±5.7%
(d) $\angle F_{r,act,N}$	∠ ± 6.6	∠ ± 25	∠ ± 5.6	∠ ± 2.5
(e) $F_r(\Theta_{drv,N})/\overline{F_{r,act,N}}$	±0.1%	±0.8%	±43%	±0.3%
(f) $\min(F_{r,act,N}/k_r)$	2.0 mm	0.66 mm	0.64 mm	2.3 mm
(g) $\max(F_{r,act,N}/k_r)$	3.5 mm	1.12 mm	1.02 mm	2.8 mm
(h) $\Delta k_{\alpha,\beta}$	±58%	±22%	±27%	±7.4%

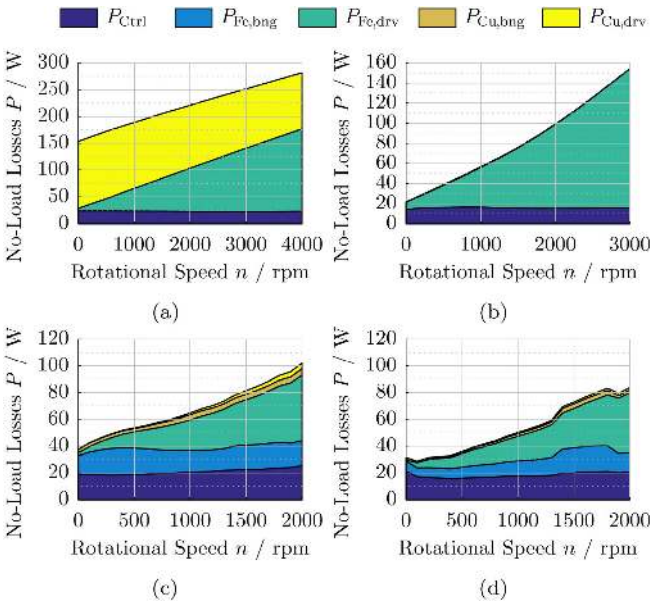

FIGURE 10. Measured no-load losses for the SynRM (a), PMSM (b), FSPM PP6 (c), and FSPM PP9 (d) operating at different rotational speeds.

D. LOSSES

Fig. 10 shows the measured no-load losses for the implemented prototypes at various rotational speeds. The components P_{Ctrl}, $P_{Fe,bng}$, $P_{Fe,drv}$, $P_{Cu,bng}$, and $P_{Cu,drv}$ denote the control/inverter losses, bearing iron losses, drive iron losses, bearing copper losses, and drive copper losses, respectively. It can be seen that the proposed SynRM topology generates the highest iron and copper losses due to the active generation of the magnetic bias flux. The shown copper losses at zero rotational speed result from the required magnetization current. A

TABLE IV Application Suitability of the Considered Motor Topologies

	SynRM	FSPM	PMSM
General, Allround	- -	- -	+ +
High Speed Rotation	+ +	-	+
High Process Temperatures	+ +	+	-
High Ambient Temperatures	+ +	-	-
Long Usage Rotor Disposable	-	+	+
Short Usage Rotor Disposable	+ +	+	- -

rotational speed of 4000 rpm can easily be achieved as there is no induced voltage caused by a PM rotor. For the PMSM the copper losses are at a negligible level and the overall no-load losses mainly consist of iron losses related to drive operation. The maximum rotational speed of 3000 rpm is limited by the back EMF in conjunction with the applied inverter voltage. While both FSPM topologies feature relatively low losses, the achievable rotational speed was limited to 2000 rpm due to stability issues of the magnetic bearing.

E. APPLICATIONS

It should be noted that the compared motor topologies vary fundamentally with regard to their mechanical and electrical construction effort, cost, and most suitable applications. The following factors should additionally be considered for a fair side-by-side comparison:

- Not all topologies are affected by the same boundary conditions, e.g., the amount of PM material that can be employed in the PMSM is limited by the rotor volume, while a weight limit of 5 kg was chosen for the FSPM.
- The considered limits restrict topologies differently, e.g., the limit of 200 W of ohmic losses has almost no effect on the FSPM topology as the iron is already saturated by the stator PMs. Contrarily, it represents a significant restriction for the SynRM as it limits the bias flux generation.
- The pole pair number was optimized for each topology in order to achieve favorable force and torque characteristics. However, different pole pair numbers result in secondary advantages and disadvantages, such as maximum rotational speed, iron losses, as well as force and torque linearity.

In order to provide an orientation regarding the most suitable application areas of the individual topologies, Table IV rates their performance regarding different requirements, based on the following evaluation criteria:

- manufacturing cost of the stator and the rotor (mainly affected by rare-earth PM volume)
- demagnetization of PMs at high temperatures (less critical for PMs in the stator)
- mechanical strength of the rotor and pole pair number (electrical frequency, harmonics).

V. CONCLUSION

An entirely magnet free bearingless synchronous reluctance slice motor (SynRM) with six stator slots and rotor flux barriers has been introduced. The feasibility of the concept has been verified by a functional prototype and a benchmarking of the achievable performance regarding various application requirements against a topology with permanent magnets in the stator (FSPM) as well as in the rotor (PMSM) has been presented. The proposed SynRM was found to provide superior performance to the FSPM with regard to passive and active magnetic forces as well as controllability. Despite the higher losses that are caused by the required active generation of the magnetic bias flux, the SynRM provides an interesting alternative to the PMSM for applications that require high speed rotation and/or high process or ambient temperatures. The cost of the rotor is low, as it contains no permanent magnet material. The switched-off motor is completely non magnetic, which simplifies the handling of the rotor. The aforementioned advantages make the proposed topology well suited for rotor disposable applications with short usage intervals, such as in the pharmaceutical industry, where the rotor is disposed together with a mixing blade in order to prevent cross contamination. In such an application, a mixing blade should be used that takes the lower tilting stiffness of the SynRM compared to the other considered topologies into account.

REFERENCES

[1] A. Chiba, T. Fukao, O. Ichikawa, M. Oshima, M. Takemoto, and D. G. Dorrell, *Magnetic Bearings and Bearingless Drives*. Amsterdam, The Netherlands: Elsevier, 2005.

[2] W. Amrhein, S. Silber, K. Nenninger, G. Trauner, M. Reisinger, and R. Schöb, "Developments on bearingless drive technology," *JSME Int. J. Ser. C Mech. Syst., Mach. Elements Manuf.*, vol. 46, no. 2, pp. 343–348, 2003.

[3] S. Silber, W. Amrhein, P. Bösch, R. Schöb, and N. Barletta, "Design aspects of bearingless slice motors," *IEEE/ASME Trans. Mechatronics*, vol. 10, no. 6, pp. 611–617, Dec. 2005.

[4] B. Liu, "Survey of bearingless motor technologies and applications," in *Proc. IEEE Int. Conf. Mechatronics Automat.*, Aug. 2015, pp. 1983–1988.

[5] A. Chiba, T. Deido, T. Fukao, and M. A. Rahman, "An analysis of bearingless AC motors," *IEEE Trans. Energy Convers.*, vol. 9, no. 1, pp. 61–68, Mar. 1994.

[6] M. Ooshima, A. Chiba, T. Fukao, and M. A. Rahman, "Design and analysis of permanent magnet-type bearingless motors," *IEEE Trans. Ind. Electron.*, vol. 43, no. 2, pp. 292–299, Apr. 1996.

[7] X. Sun, L. Chen, and Z. Yang, "Overview of bearingless permanent-magnet synchronous motors," *IEEE Trans. Ind. Electron.*, vol. 60, no. 12, pp. 5528–5538, Dec. 2013.

[8] W. Gruber, W. Briewasser, M. Rothböck, and R. T. Schöb, "Bearingless slice motor concepts without permanent magnets in the rotor," in *Proc. IEEE Int. Conf. Ind. Technol.*, Feb. 2013, pp. 259–265.

[9] A. Chiba, K. Kiyota, N. Hoshi, M. Takemoto, and S. Ogasawara, "Development of a rare-earth-free SR motor with high torque density for hybrid vehicles," *IEEE Trans. Energy Convers.*, vol. 30, no. 1, pp. 175–182, Mar. 2015.

[10] G. Pellegrino, T. M. Jahns, N. Bianchi, W. L. Soong, and F. Cupertino, *The Rediscovery of Synchronous Reluctance and Ferrite Permanent Magnet Motors: Tutorial Course Notes*. Berlin, Germany: Springer, 2016.

[11] J. Estima and A. Cardoso, "Super premium synchronous reluctance motor evaluation," in *Proc. Int. Conf. Energy Efficiency Motor Driven Syst.*, 2013, pp. 213–222.

[12] K. Urase *et al.*, "Energy efficiency of SR and IPM generators for hybrid electric vehicle," *IEEE Trans. Industry Appl.*, vol. 51, no. 4, pp. 2874–2883, Jul. 2015.
[13] M. Takemoto, K. Yoshida, N. Itasaka, Y. Tanaka, A. Chiba, and T. Fukao, "Synchronous reluctance type bearingless motors with multi-flux barriers," in *Proc. Power Convers. Conf. Nagoya*, Apr. 2007, pp. 1559–1564.
[14] M. Takemoto, H. Suzuki, A. Chiba, T. Fukao, and M. A. Rahman, "Improved analysis of a bearingless switched reluctance motor," *IEEE Trans. Industry Appl.*, vol. 37, no. 1, pp. 26–34, Jan. 2001.
[15] V. Mukherjee, J. Pippuri, S. E. Saarakkala, A. Belahcen, M. Hinkkanen, and K. Tammi, "Finite element analysis for bearingless operation of a multi flux barrier synchronous reluctance motor," in *Proc. 18th Int. Conf. Elect. Mach. Syst.*, Oct. 2015, pp. 688–691.
[16] S. E. Saarakkala *et al.*, "Flux-linkage model including cross-saturation for a bearingless synchronous reluctance motor," in *Proc. ISMB15*, 2016, pp. 501–508.
[17] H. Ding, H. Zhu, and Y. Hua, "Optimization design of bearingless synchronous reluctance motor," *IEEE Trans. Appl. Supercond.*, vol. 28, no. 3, Apr. 2018, Art. no. 5202905.
[18] X. Diao, H. Zhu, Y. Qin, and Y. Hua, "Torque ripple minimization for bearingless synchronous reluctance motor," *IEEE Trans. Appl. Supercond.*, vol. 28, no. 3, Apr. 2018, Art. no. 5205505.
[19] A. Belahcen, V. Mukhrejee, F. Martin, and P. Rasilo, "Computation of hysteresis torque and losses in a bearingless synchronous reluctance machine," *IEEE Trans. Magn.*, vol. 54, no. 3, Mar. 2018, Art. no. 7300804.
[20] J. Rao, W. Hijikata, and T. Shinshi, "A bearingless motor utilizing a permanent magnet free structure for disposable centrifugal blood pumps," *J. Adv. Mech. Des., Syst. Manuf.*, vol. 9, no. 3, 2015, Art. no. JAMDSM0046.
[21] M. Sokolov, W. Gruber, S. E. Saarakkala, and M. Hinkkanen, "Modeling of a bearingless synchronous reluctance motor with combined windings," in *Proc. IEEE Energy Convers. Congr. Expo.*, 2019, pp. 7084–7090.
[22] T. Holenstein, J. Greiner, D. Steinert, and J. W. Kolar, "A high torque, wide air gap bearingless motor with permanent magnet free rotor," in *Proc. IEEE Int. Electric Mach. Drives Conf.*, May 2017, pp. 1–6.
[23] T. Holenstein, T. Nussbaumer, and J. W. Kolar, "A bearingless synchronous reluctance slice motor with rotor flux barriers," in *Proc. Int. Power Electron. Conf. (IPEC-Niigata ECCE Asia)*, May 2018, pp. 3619–3626.
[24] H. Mitterhofer, W. Gruber, and W. Amrhein, "On the high speed capacity of bearingless drives," *IEEE Trans. Ind. Electron.*, vol. 61, no. 6, pp. 3119–3126, Jun. 2014.
[25] S. Silber, J. Sloupensky, P. Dirnberger, M. Moravec, W. Amrhein, and M. Reisinger, "High-speed drive for textile rotor spinning applications," *IEEE Trans. Ind. Electron.*, vol. 61, no. 6, pp. 2990–2997, Jun. 2014.
[26] J. Asama, T. Tatara, T. Oiwa, and A. Chiba, "Suspension performance of a two-DoF actively positioned consequent-pole bearingless motor with a wide magnetic gap," in *Proc. IEEE Int. Electric Mach. Drives Conf.*, May 2015, pp. 786–791.
[27] H. Sugimoto, Y. Uemura, A. Chiba, and M. A. Rahman, "Design of homopolar consequent-pole bearingless motor with wide magnetic gap," *IEEE Trans. Magn.*, vol. 49, no. 5, pp. 2315–2318, May 2013.
[28] D. Steinert, T. Nussbaumer, and J. W. Kolar, "Slotless bearingless disk drive for high-speed and high-purity applications," *IEEE Trans. Ind. Electron.*, vol. 61, no. 11, pp. 5974–5986, Nov. 2014.
[29] H. Bleuler, *et al.*, *Magnetic Bearings: Theory, Design, and Application to Rotating Machinery*. Berlin, Germany: Springer, 2009.
[30] H. Sugimoto, M. Miyoshi, and A. Chiba, "Axial vibration suppression by field flux regulation in two-axis actively positioned permanent magnet bearingless motors with axial position estimation," *IEEE Trans. Industry Appl.*, vol. 54, no. 2, pp. 1264–1272, Mar./Apr. 2018.
[31] M. Cheng, W. Hua, J. Zhang, and W. Zhao, "Overview of stator-permanent magnet brushless machines," *IEEE Trans. Ind. Electron.*, vol. 58, no. 11, pp. 5087–5101, Nov. 2011.
[32] T. Reichert, T. Nussbaumer, and J. W. Kolar, "Bearingless 300-W PMSM for bioreactor mixing," *IEEE Trans. Ind. Electron.*, vol. 59, no. 3, pp. 1376–1388, Mar. 2012.
[33] B. Warberger, R. Kaelin, T. Nussbaumer, and J. W. Kolar, "50- /2500-W bearingless motor for high-purity pharmaceutical mixing," *IEEE Trans. Ind. Electron.*, vol. 59, no. 5, pp. 2236–2247, May 2012.

THOMAS HOLENSTEIN (Student Member, IEEE) was born in 1984 in St. Gallen, Switzerland, received the M.Sc degree in electrical engineering and information technology from the ETH Zurich, Switzerland, in 2009. During his studies, he focused on power electronics and mechatronics. In his master thesis, he developed new control algorithms for magnetically levitated motors. Since 2010 he is working as an R&D Engineer with the company Levitronix. Since 2015 he is a Ph.D. Student at the Power Electronic Systems Laboratory, ETH Zurich, where he is working on new motor concepts for magnetically levitated single-use drives.

MARCEL SCHUCK (Member, IEEE) received the B.Sc. degree in electrical and computer engineering from the Technische Universität Darmstadt, Germany, in 2011 and the M.Sc. degree in the same field from the University of Illinois at Urbana-Champaign in 2013. He received an MBA degree from the Collège des Ingénieurs in Paris, France in 2014. He was a Ph.D. Student at the Power Electronic Systems Laboratory at ETH Zurich, Switzerland from 2014 to 2017, where he is currently working as a Postdoctoral Researcher. His research interests include ultra-high speed bearingless machines, acoustic levitation, and mechatronic systems.

JOHANN W. KOLAR (Fellow, IEEE) received the M.Sc. and Ph.D. degrees (summa cum laude) from the Vienna University of Technology, Vienna, Austria. He is currently a Full Professor with and the Head of the Power Electronic Systems Laboratory, Swiss Federal Institute of Technology Zurich (ETH Zurich), Zurich, Switzerland. He has proposed numerous novel pulsewidth-modulation converter topologies and modulation and control concepts, published more than 650 scientific papers in international journals and conference proceedings, and filed more than 110 patents. The focus of his current research is on ultracompact and ultraefficient converter topologies employing latest power semiconductor technology (SiC and GaN), wireless power transfer, solid-state transformers, power supplies on chip, and ultra-high speed and bearingless motors. Prof. Kolar was a recipient of 21 IEEE Transactions and conference prize paper awards, the 2014 SEMIKRON Innovation Award, the 2014 IEEE Power Electronics Society R. David Middlebrook Award, and the ETH Zurich Golden Owl Award for Excellence in Teaching.